Cosmic axions revealed via amplified modulation of the ellipticity of a laser

Hooman Davoudiasl[1] and Yannis K. Semertzidis[2,*]

[1]*High Energy Theory Group, Physics Department, Brookhaven National Laboratory, Upton, New York 11973, USA*

[2]*Department of Physics, Korea Advanced Institute of Science and Technology (KAIST), Daejeon 34141, Republic of Korea*

(Received 25 August 2025; accepted 20 January 2026; published 17 February 2026)

We propose a new axion dark matter detection strategy that employs optical readout of laser beam ellipticity modulations caused by axion-induced electric fields in a microwave cavity, using electro-optic (EO) crystals, enhanced by externally injected radio-frequency (rf) power. Building upon the variance-based probing method [Phys. Rev. D **107**, 103005 (2023).], we extend this concept to the optical domain: A weak probe laser interacts with an EO crystal coupled to the resonant microwave cavity field at cryogenic temperatures, and the axion-induced electric field is revealed through induced ellipticity. The injected rf signal coherently interferes with that of the axion field, amplifying the optical response and significantly improving sensitivity. While our EO-based method employs a Fabry-Pérot resonator, we do not require Michelson interferometers. Our method, hence, enables compact, high-frequency axion searches, across the 0.5–50 GHz range. Operating at cryogenic temperatures not only suppresses thermal backgrounds, but, critically, allows the probing method to mitigate the quantum noise. This approach offers a scalable path forward for axion detection over the $\sim(\text{few}-200)\,\mu\text{eV}$ mass range—covering the preferred parameter space for the postinflationary Peccei-Quinn axion dark matter—using compact, tunable systems.

DOI: 10.1103/2dvg-78kh

I. INTRODUCTION

The identity of dark matter (DM) remains one of the most compelling unsolved problems in fundamental physics. Among the theoretically favored candidates is the quantum chromodynamics (QCD) axion a [1,2], associated with the Peccei-Quinn (PQ) mechanism [3,4] originally introduced to resolve the strong CP problem, i.e., the puzzling smallness of the CP-violating parameter in QCD. The axion of the PQ framework emerges as a natural cold dark matter candidate, with its abundance determined by early-Universe dynamics [5–7]. For a recent article on the resilience of the strong CP problem, see Ref. [8].

The mass m_a of the QCD axion DM is expected to have a narrow viable range if the associated PQ symmetry is broken after inflation in the early Universe (see, for example, Ref. [9]). Cosmological and lattice calculations suggest that postinflationary scenarios prefer an axion mass in the tens to hundreds of μeV [10–15] range, with a recent analysis suggesting $40\ \mu\text{eV} < m_a < 180\ \mu\text{eV}$ [16]. This mass range can be well covered by resonant cavity technique proposed below, in the photon frequency range 0.5–50 GHz, which will be the focus of our discussion.

The most sensitive experimental approach to detecting axions in the above mass window is the haloscope technique, which exploits axion-photon conversion in a resonant microwave cavity permeated by a strong magnetic field, as was suggested first by Sikivie [6]. However, haloscopes face a fundamental limitation: As the resonant frequency increases, the physical volume of the cavity—and, hence, the signal power—must decrease. For an axion signal at 25 GHz, a natural cavity volume is $\sim 1\ \text{cm}^3$, over $10^5\times$ smaller than the volumes used in the original ADMX configuration [17–22]. Covering the 0.5–50 GHz range at half the resolution matched to the axion coherence bandwidth, $\Delta\nu/\nu \sim 10^{-6}$, requires $\sim 10^7$ distinct frequency channels (the bandwidth for axions is set by their small kinetic energy $\propto v^2$, where $v \sim 10^{-3}$ is the virial velocity in our Galactic neighborhood). This scaling imposes a stringent limitation on scanning speed, primarily because conventional readout electronics contribute significant quantum or thermal noise, requiring long integration times per frequency channel. For example, assuming a typical ∼100 s integration time per bin, covering the above frequency range would take ∼30 yr. By contrast, our proposed axion signal probing method, based on laser readout through a

*Contact author: yannis@bnl.gov

Published by the American Physical Society under the terms of the Creative Commons Attribution 4.0 International license. Further distribution of this work must maintain attribution to the author(s) and the published article's title, journal citation, and DOI. Funded by SCOAP³.

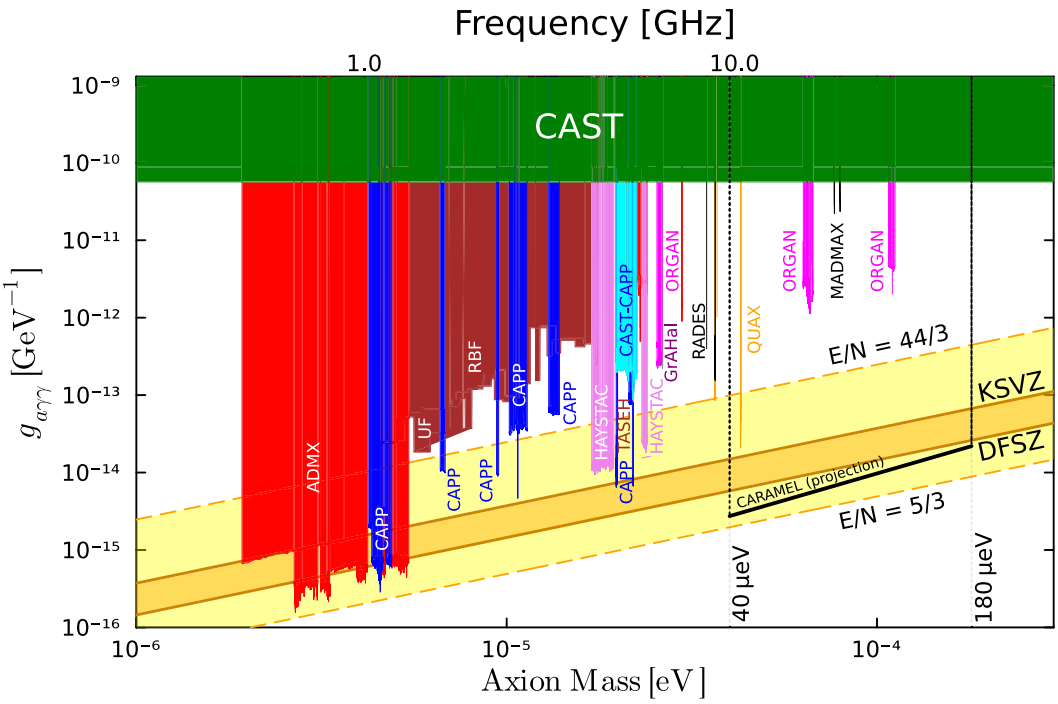


FIG. 1. The current status of the axion to two-photon coupling in the mass range $1-300$ μeV, corresponding to the frequency range 0.2–70 GHz (from Ref. [23], ADMX [17,19,22,27–29], ADMX-Sidecar [30,31], ADMX-SLIC [32], CAPP [33–44], CAST [45–47], CAST-CAPP [48], GrAHal [49], HAYSTAC [50–54], MADMAX [55], ORGAN [56–59], QUAX [60–64], RADES [65,66], RBF [67,68], TASEH [69], and UF [70,71]). CARAMEL aims to facilitate probing the frequency range of 0.5–50 GHz, or ∼ (2–200) μeV, with better than DFSZ sensitivity within the next five years. CARAMEL can potentially cover the preferred postinflationary axion parameter space, corresponding to $40-180$ μeV [16], with better than DFSZ sensitivity using presently available technical capabilities. The projected sensitivity curve in this mass range corresponds to a total scanning time of approximately 2×10^7 s, which includes both data acquisition (3 s) and cavity retuning (3 s) per frequency step, assuming frequency steps of half the axion linewidth. The projection further assumes a constant axion-to-photon conversion power of 10^{-21} W and a cavity quality factor of $Q_c = 10^6$ across the indicated mass range (equivalent to 10^{-23} W for a quality factor of $Q_c = 10^4$).

Fabry-Pérot interferometer and electro-optic modulation, effectively bypasses the limitations of traditional rf electronics. It enables sensitivity well beyond the quantum noise floor typically imposed by the detection system. The method proposed here can potentially speed up scanning rates by more than an order of magnitude, using available technology.

Current state-of-the-art experiments in this regime rely on ultralow-noise amplifiers, quantum-limited detectors, and often large optical interferometers or complex cavity geometries. Yet, sensitivity improvements remain incremental, and the ability to scan efficiently across millions of channels with sufficient signal-to-noise ratio (SNR) remains out of reach. A fundamentally different approach is required to break through this bottleneck—one that enables enhanced sensitivity even in small volumes, with suppressed noise, and minimal reliance on ultracomplex cryogenic amplification chains.

The current status of axion searches is summarized by the plot in Fig. 1, taken from Ref. [23]. As can be seen here, the window corresponding to the preferred postinflationary PQ axion DM, $\sim 40-180$ μeV, within the Kim–Shifman–Vainshtein–Zakharov (KSVZ) [24,25] and Dine–Fischler–Srednicki–Zhitnitsky (DFSZ) [7,26] scenarios, remains largely unexplored. This hints at the inherent challenges associated with this regime of parameters. Progress in this range has been slow due to the convergence of several technical challenges: The cavity volume decreases with increasing frequency, conventional copper cavities suffer from degraded quality factors at high frequencies, and quantum-limited linear amplifiers constrain the readout sensitivity. Meanwhile, single-photon detectors, though promising, are not yet mature for robust operation under realistic laboratory conditions.

To overcome these barriers, multiple high-frequency haloscope concepts are under active development. These include the pizza-cavity design [72], which partitions the cavity into multiple sectors to increase frequency while preserving volume efficiency; photonic crystal [73,74] and metamaterial cavities [75], which decouple frequency from physical size; and horn-array haloscopes [76], which leverage large metal surface areas to achieve broadband, volume-efficient searches at high frequencies. Additionally, pioneering experiments such as MADMAX [77–79] and DALI [80] explore dielectric haloscope techniques

using layered dielectric interfaces to coherently boost the axion-induced signal power. The ORGAN experiment [81–83] utilizes tunable resonant cavities in high magnetic fields to target axions in the 15–50 GHz range with ultralow-noise quantum-limited readout systems. ALPHA uses the electron plasma resonance frequency of metallic rods [84], and CAST-CAPP [85] employed a decommissioned dipole magnet in an efficient geometry. Superconducting cavities with quality factors comparable to or exceeding the expected axion quality factor, even in the presence of strong magnetic fields (∼8 T and above), have been demonstrated using high-temperature superconducting tapes [86–88]. These developments indicate that this technology is maturing and offers a scalable path toward detecting axions in the tens to hundreds of μeV mass range, as motivated by postinflation QCD axion models.

In parallel, we introduce cosmic axions revealed via amplified modulation of the ellipticity of a laser (CARAMEL), a novel detection technique that mitigates the effects of quantum noise and replaces conventional amplifier chains with optical readout. CARAMEL detects the axion-induced microwave field via its modulation of a laser beam polarization or phase, thus bypassing the quantum noise limitations of linear amplification. Importantly, this method is not limited to high frequencies: It can also be applied at lower frequencies (e.g., near 200 MHz), where electronic noise in standard amplifiers is still far above the quantum limit. In these cases, CARAMEL can yield sensitivity improvements of up to several orders of magnitude, making it a transformative technique for axion detection across the full spectrum from subgigahertz to tens of gigahertz.

Our proposal combines electro-optic (EO) detection [89] and a "resonant probing" technique [90]; see also [91–93]. These methods, previously suggested independently, are now unified to offer

(1) sensitivity mitigating the quantum noise limit at low temperatures and.
(2) operation with only modest laser power (10 mW).

This approach is also applicable to other experimental geometries, including MADMAX and related dielectric haloscope designs [77–80,84].

Next, we will discuss the basics of the axion detection in our proposed setup. We will provide estimates for the signal and main sources of noise. Our analysis will illustrate that the SNR achieved can lead to a definitive detection across and beyond the postinflationary PQ axion DM parameter space, employing technology that is currently available. Henceforth, we shall assume a laser with power $P = 10\ \text{mW} = 10^{-2}\ \text{W}$ and wavelength $\lambda = 1064\ \text{nm} \Rightarrow \nu = c/\lambda \approx 2.82 \times 10^{14}\ \text{Hz}$, where ν is the laser beam frequency; $h = 6.626 \times 10^{-34}\ \text{J s}$ is Planck's constant.

II. DETECTION PRINCIPLE

The basis of our proposal is the use of the EO effect, where an electric field $E \equiv |\vec{E}|$ leads to induced ellipticity ψ in a laser beam of wavelength λ (Pockels effect [94,95]). We have

$$\psi = \frac{\pi}{\lambda} n^3 r_{ij} E L_c, \tag{1}$$

where n is refractive index of the EO crystal, r_{ij} is assumed to be the largest element of the EO coefficient tensor, and L_c is the length of the crystal through which the laser propagates.

Let us now estimate the contribution of axion conversion in a cavity to the above effect. The power output from axion-to-photon conversion in a microwave cavity operating in the TM_{010} mode, using experimental parameters as reported by CAPP, is given by [43,96]

$$\begin{aligned} P_{a\gamma\gamma} = 8.7 \times 10^{-23}\ \text{W} &\left(\frac{g_\gamma}{0.36}\right)^2 \left(\frac{\rho_a}{0.45\ \text{GeV/cm}^3}\right) \\ &\times \left(\frac{\nu_a}{1.1\ \text{GHz}}\right)\left(\frac{\langle \mathbf{B}_e^2 \rangle}{(10.3\text{T})^2}\right)\left(\frac{V}{37\text{L}}\right) \\ &\times \left(\frac{G}{0.6}\right)\left(\frac{10^6}{Q_a} + \frac{10^5}{Q_c}\right)^{-1}, \end{aligned} \tag{2}$$

where $g_{a\gamma\gamma} = (\alpha/\pi)(g_\gamma/f_a)$ is the axion-photon coupling, α is the fine structure constant, and g_γ takes values of -0.97 (KSVZ model [24,25]) or 0.36 (DFSZ model [7,26]). f_a is the PQ symmetry-breaking scale, also known as the decay constant. ρ_a is the local axion dark matter density, and $\nu_a = m_a c^2/h$ is the axion Compton frequency ($c = 2.998 \times 10^8$ m/s is the speed of light). In the above, $\langle \mathbf{B}_e^2 \rangle$ is the squared average external magnetic field, V is the cavity volume, $Q_a \approx 10^6$ is the axion quality factor, and Q_c is the cavity unloaded quality factor. The form factor G reflects the mode-dependent overlap of the axion-induced field with the resonant mode and is approximately 0.69 for the TM_{010} mode.

In the limit $Q_c \ll Q_a$, the signal power scales linearly with Q_c:

$$P_a \propto Q_c. \tag{3}$$

Conversely, for $Q_c \gg Q_a$, the signal power saturates:

$$P_a \approx (\text{const}) \propto Q_a, \tag{4}$$

reflecting the finite spectral width of the axion signal; the cavity cannot enhance the signal beyond the axion's intrinsic coherence bandwidth.

The total power deposited by axion conversion is given by

TABLE I. Benchmark parameters assumed in this work for the representative regime $\nu_a \sim \mathcal{O}(10\ \mathrm{GHz})$. These parameters are employed throughout the main text as a reference operating point to illustrate the scaling and performance of the proposed method and are not unique or restrictive. A more general and experimentally flexible parameter range, consistent with all system-level requirements—including optical absorption, rf dissipation, and cryogenic heat-loading constraints—is presented in Appendix D and summarized in Table II.

Parameter	Value
Laser power	10 mW
Laser wavelength	1064 nm
rf probe power	2 nW
Microwave cavity quality factor Q_c	10^4
Axion-to-photon reference power P_a, for $Q_c = 10^4$	10^{-23} W
Microwave cavity volume	3.7 L
Fabry-Pérot finesse $\mathcal{F}$	10^4
EO crystal ($LiNbO_3$) thickness L_c	3 mm

$$P_a = \frac{\omega U}{Q_c}, \tag{5}$$

where P_a is the axion-induced power in Eq. (2), $\omega = 2\pi\nu$ is the angular frequency of the cavity (or the axion, on resonance), and U is the total stored energy in the cavity. Since the stored energy is equally partitioned between electric and magnetic components, the electric field energy is [97]

$$U_E = \frac{1}{2}\epsilon_0 V E_a^2 = \frac{U}{2} = \frac{P_a Q_c}{2\omega}, \tag{6}$$

where E_a is the root-mean-square electric field, $\epsilon_0 = 8.85 \times 10^{-12}$ F/m is the vacuum permittivity, and V is the cavity volume. Solving for E_a, we get

$$E_a = \sqrt{\frac{P_a Q_c}{\omega \epsilon_0 V}}. \tag{7}$$

We will use $V = 3.7 \times 10^{-3}$ m^3 (3.7 liters) as a benchmark value in what follows, appropriate for a modified 10 GHz cavity. However, this volume is not a fixed requirement. At a given frequency, the cavity geometry may be adapted to vary V while maintaining resonance to satisfy a desired reference power level. This flexibility in cavity volume is particularly useful for optimizing sensitivity while staying within the physical constraints imposed by the detection scheme and available magnet apertures.

We will consider using lithium niobate, $LiNbO_3$, of size $L_c = 3$ mm, as our EO crystal, for which $n \approx 2.2$ and $r_{33} \approx 3.1 \times 10^{-11}$ m/V. Let us take $\nu = 10$ GHz as a representative value, with all the benchmark parameters used in this document shown in Table I. We will consider the benchmark values $P_a = 10^{-23}$ W and $Q_c = 10^4$ for the chosen value of ν above. From Eqs. (1) and (7), we get $E_a \approx 7.0 \times 10^{-9}$ V/m and $\psi_a \approx 2 \times 10^{-14}$ rad.

To determine the minimum detectable ellipticity, we need to estimate contributions from various sources of noise. We identify two main sources: (i) shot noise from the finite power output of the laser beam and (ii) the quantum-thermal noise in the cavity. Here, we first examine the effect of shot noise and in the next subsection we will discuss quantum-thermal effects.

(i) Shot noise. To estimate the photon shot noise, we use the standard expression

$$\delta\psi_{\text{shot-laser}} = \frac{\sqrt{2}}{\sqrt{P/h\nu}} = \sqrt{\frac{2h\nu}{P}}, \tag{8}$$

where P is the laser power and ν is the associated frequency. Substituting our benchmark values, we have

$$\delta\psi_{\text{shot-laser}} \approx 6.1 \times 10^{-9}\ \text{rad} \cdot \text{Hz}^{-1/2}. \tag{9}$$

For an integration time of $t = 3$ s, assumed henceforth, we get (see Appendix A)

$$\delta\psi_{\text{shot-laser}} = \frac{6.1 \times 10^{-9}}{\sqrt{3}} \approx 3.5 \times 10^{-9}\ \text{rad}. \tag{10}$$

Assuming only laser beam shot noise, we see that the expected typical SNR would be

$$\text{SNR}_{\text{laser}} = \frac{\psi_a}{\delta\psi_{\text{shot}}} \approx 6 \times 10^{-6}, \tag{11}$$

which is quite tiny.

If we consider detection using only the axion-induced electric field E_a, a Fabry-Pérot (FP) cavity with finesse $\mathcal{F} = 10^4$ can boost the signal according to

$$\psi_a \to \left(\frac{2\mathcal{F}}{\pi}\right)\psi_a \approx 1.3 \times 10^{-10}\ \text{rad}, \tag{12}$$

that would yield an $\text{SNR}_{\text{FP}} \sim 0.04$, which is insufficient for detection. However, we will see next how using a probe radio-frequency (rf) beam at the axion frequency of oscillation can further enhance the signal.

A. Probing method with electro-optic readout

The axion-induced oscillating electric field modulates the birefringence of the EO crystal, imprinting a small ellipticity or phase shift onto the laser polarization. To enhance the readout signal, we introduce an rf tone at the cavity resonance frequency, which coherently interferes with the axion-induced field inside the cavity. The probing method effectively amplifies the signal by creating a beat between the injected rf field and the axion signal, leading to

a variance in the optical response that is detectable with high sensitivity. This technique, originally developed for microwave detection using power detectors [90], is applied in the EO axion signal detection here, for the first time.

Since the detection occurs via polarization rotation (ellipticity) in the optical field—not via amplification of the microwave field itself—the signal readout is not constrained by the standard quantum limit. Furthermore, because the probing method effectively decouples the signal strength from the laser power, the system can operate at low optical intensities, minimizing thermal loading on the cryogenic environment.

Operating at cryogenic temperatures ($T \lesssim 100$ mK), the thermal photon background for a single-photon detector is exponentially suppressed. However, quantum field fluctuations still exist for the method suggested here, albeit significantly reduced. Combined with the narrow bandwidth of a high-Q_c cavity, this results in a low-noise environment ideal for detecting weak axion-induced fields. The result is a highly sensitive, compact, and scalable architecture for axion detection in the 0.5–50 GHz range; in principle, the lower range can be further reduced.

Next, we will examine implementing the probing method to provide a feasible detection approach, without FP enhancement. We will consider an injected rf power $P = 2$ nW $= 2 \times 10^{-9}$ W. The electric field amplitude, for $\omega = 2\pi \times 10^{10}$ rad/s, $V = 3.7$ L, and $Q_c = 10^4$ is

$$E_{\rm probe} = \sqrt{\frac{Q_c P}{\epsilon_0 V \omega}} \approx 0.1 \text{ V/m}. \tag{13}$$

In the probing method, we are interested in detecting the fluctuations of the ellipticity, which are enhanced by the rf injected power. To see this, we note that the total electric field in the cavity is given by

$$E(t) = E_{\rm probe}\cos(\omega t) + E_a \cos(\omega t + \phi(t)), \tag{14}$$

where $\phi(t)$ is the time-dependent relative phase between the two fields.

The axion field is not perfectly monochromatic; it has a finite spectral width $\Delta\nu_a \sim 10^{-6}\nu$ due to the virialized velocity dispersion of dark matter in the galactic halo. At $\nu = 10$ GHz, this corresponds to $\Delta\nu_a \sim 10$ kHz and a coherence time of

$$\tau_a \sim \frac{1}{\Delta\nu_a} \sim 0.1 \text{ ms}. \tag{15}$$

Over timescales shorter than τ_a, the axion field behaves like a coherent wave with a well-defined phase. Over longer timescales, this phase $\phi(t)$ drifts randomly, reflecting the stochastic nature of the axion field.

In the probing method, one is interested in measuring the variance of the ellipticity

$$\langle \psi^2 \rangle \propto \frac{1}{2}[E_{\rm probe}^2 + E_a^2 + 2E_{\rm probe}E_a\langle\cos(\phi(t))\rangle], \tag{16}$$

where $\langle\cos(\phi(t))\rangle$ vanishes over many coherence times but the variance of the fluctuations is nonzero. To capture these fluctuations, one needs to have a sampling timescale $t_{\rm sample} \lesssim \tau_a$. In the above expression (16), fast axion oscillations at $\omega \sim m_a$ have been averaged out, since they take place at timescales much shorter than $t_{\rm sample}$. Physically, the probe tone mixes coherently with the axion-induced field to generate a beat signal at the difference frequency—typically in the 1–50 kHz range. This beat modulates the birefringence of the electro-optic crystal at a frequency far below the carrier, allowing low-frequency optical detection of an otherwise extremely weak GHz signal.

Given the above discussion, the detected ellipticity scales with the geometric mean of the axion and probe electric fields:

$$\psi_{\rm probe} = \frac{\pi}{\lambda} n^3 r_{33} \sqrt{E_a E_{\rm probe}} L_c. \tag{17}$$

Substituting the above benchmark values, we find $\psi_{\rm probe} \approx 7.7 \times 10^{-11}$ rad. As before, if we employ a FP cavity with a finesse $\mathcal{F}$, we can enhance the signal:

$$\psi_{\rm probe} \to \left(\frac{2\mathcal{F}}{\pi}\right)\psi_{\rm probe}, \tag{18}$$

which for $\mathcal{F} = 10^4$ will result in $\psi_{\rm probe} \approx 4.9 \times 10^{-7}$ rad.

Thus, the SNR for a 10 mW laser power and integrating for 3 s, is

$$\text{SNR}_{\text{probe-FP}} \approx \frac{(2\mathcal{F}/\pi)\psi_{\rm probe}}{\delta\psi_{\rm shot}} \approx \frac{4.9 \times 10^{-7}}{3.5 \times 10^{-9}} \approx 140. \tag{19}$$

We see, from the above, that a combination of probing and FP enhancement allows for a detectable signal, easily overcoming the measurement limitations. In fact, given the size of the above SNR, we could envision that a lower laser beam power, in conjunction with a thinner EO crystal, would also suffice for the measurement.

Here, we would like to make the following two points. First, as mentioned earlier, due to the probing method, the required sampling time is set by the axion coherence time $\tau_a = Q_a/\nu$, which is ~10 kHz, about 6 orders of magnitude below the axion frequency. Secondly, the rf probe affects both the axion signal and the quantum-thermal background. This suggests that we need to examine the associated effective SNR for the measurement further, which will do next.

B. rf probe effect on sensitivity

Vacuum fluctuations of the electromagnetic field, though classically absent, have measurable consequences in quantum electrodynamics. In particular, they give rise to the zero-point energy of each electromagnetic mode, with an average energy of $\hbar\omega/2$, and manifest as nonzero field quadratures even at zero temperature. Single-photon detectors are sensitive only to real (on-shell) photons through energy absorption, and, hence, they remain insensitive to these vacuum fluctuations. However, we would need to account for such off-shell effects, as discussed below.

(ii) Quantum-thermal noise. The average number of thermal photons in the cavity mode is

$$\bar{n}_{\rm th} = \frac{1}{e^{\hbar\omega/k_B T} - 1}, \tag{20}$$

where $k_B = 1.38 \times 10^{-23}$ J/K is the Boltzmann constant. Each photon contributes an energy $\hbar\omega$, with $\hbar \equiv h/(2\pi)$, so the thermal energy associated with the cavity is

$$U_{\rm th} = \hbar\omega\left(\bar{n}_{\rm th} + \frac{1}{2}\right) \tag{21}$$

with the half photon constant background present due to off-shell vacuum fluctuations.

This energy is equally partitioned between the electric and magnetic fields, so the electric field energy is

$$U_E = \frac{1}{2} U_{\rm th}. \tag{22}$$

The above energy can also be expressed in terms of the electric field amplitude as

$$U_E = \frac{1}{2}\epsilon_0 V E_{\rm th}^2. \tag{23}$$

Solving for the electric field $E_{\rm th}$ yields

$$E_{\rm th} = \sqrt{\frac{U_{\rm th}}{\epsilon_0 V}} = \sqrt{\frac{(\bar{n}_{\rm th} + 1/2)\hbar\omega}{\epsilon_0 V}}, \tag{24}$$

which represents the root-mean-square electric field amplitude of the thermal plus quantum fluctuations in the cavity. This sets the quantum noise floor for field-based detection methods.

The axion-induced power is

$$P_a = P_0 Q_{\rm red}, \tag{25}$$

where P_0 is a reference quantity and the reduced quality factor given by

$$Q_{\rm red} \equiv \frac{Q_c Q_a}{Q_c + Q_a}. \tag{26}$$

For our benchmark choices $P_0 = 10^{-27}$ W, for $Q_c = 10^4$. The stored electric field amplitude in the resonant cavity is given by Eq. (7), as derived before:

$$E_a = \sqrt{\frac{P_a Q_c}{\epsilon_0 V \omega}}.$$

Assuming an axion coherence time $\tau_a = Q_a/\nu$, the SNR due to thermal noise after an integration time t is given by

$$\mathrm{SNR}_{\rm th}(t) = \frac{E_a}{E_{\rm th}} \cdot \sqrt{\frac{t}{\tau_a}}, \tag{27}$$

which yields

$$\mathrm{SNR}_{\rm th}(t) = \sqrt{\frac{P_0 Q_{\rm red} Q_c t}{2\pi(\bar{n}_{\rm th} + \frac{1}{2})\hbar\omega Q_a}}, \tag{28}$$

valid when $Q_c \le Q_a$. Equation (28) treats the full cavity bandwidth as contributing thermal noise and, therefore, provides only an approximate estimate. In practice, only the noise within the axion (or beat-note) linewidth is relevant, introducing a bandwidth factor $\sqrt{Q_c/Q_a}$ that Eq. (28) does not include. The complete treatment in Appendix B, [Eq. (B17)] provides

$$\mathrm{SNR}(t) = \sqrt{\frac{P_0 Q_{\rm red} t}{\pi\hbar\omega \coth(\frac{\hbar\omega}{2k_B T})}}. \tag{29}$$

This expression smoothly interpolates between the quantum regime at low temperatures [where $\coth(\hbar\omega/2k_B T) \to 1$ as $T \to 0$] and the classical limit at high temperatures [where $\coth(\hbar\omega/2k_B T) \to 2k_B T/\hbar\omega$ as $T \to \infty$].

As detailed in the Appendixes B and D, the thermal noise field contributing to signal detection is not determined solely by the total thermal energy stored in the cavity mode but by the fraction of this energy that spectrally overlaps with the axion signal bandwidth. In the regime where the cavity quality factor is much smaller than the axion coherence quality factor ($Q_c \ll Q_a$), only thermal fluctuations within a bandwidth $\Delta\nu \sim \nu/Q_a$ contribute effectively to the signal readout. This leads to a suppression of the thermal noise electric field amplitude by a factor $\sqrt{Q_c/Q_a}$, since the axion signal is narrow band while the cavity noise is broadband. The probing method, by isolating this narrow interference bandwidth, enables a higher SNR despite a broad cavity response. Figure 2 illustrates this effect for the representative case at 10 GHz, showing how SNR depends on both temperature and cavity quality factor and

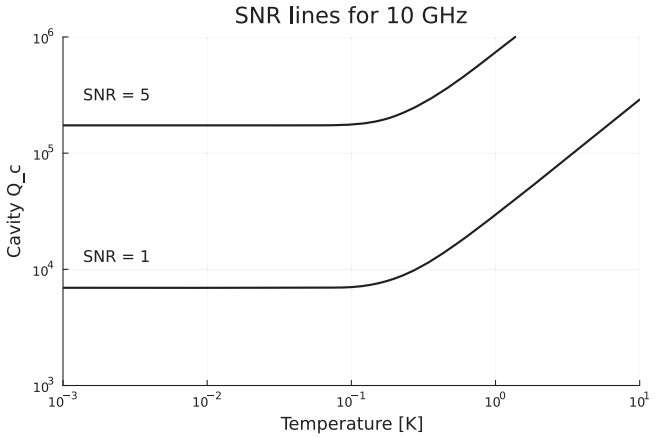


FIG. 2. SNR as a function of Q_c and T at different operating frequencies. The transition from the quantum regime to the classical regime becomes apparent around 480 mK, where the thermal photon occupation number begins to exceed the vacuum (zero-point) contribution. The cavity volume is kept constant at 3.7 liters. The axion to photon conversion power is kept at 10^{-23} W assuming $Q_c = 10^4$, $t = 3$ s, and scaled appropriately for different cavity quality factor values; see Appendixes B and D.

highlighting the transition between quantum and classical thermal noise regimes.

The $\sqrt{Q_c/Q_a}$ thermal noise suppression can also be recovered without probing, provided that the cavity output is analyzed with frequency resolution matched to the axion linewidth $\Delta\nu_a = \nu/Q_a$. In this case, only the thermal noise within a single high-resolution Fourier transform bin contributes, and the SNR expression remains equivalent. However, the probing method achieves the same filtering effect automatically through beat-based detection.

III. DISCUSSION: SURPASSING THE LASER QUANTUM NOISE LIMIT OF LINEAR MICROWAVE AMPLIFICATION

The combination of the probing method—where a known rf signal is injected into the system—and FP enhancement enables a substantial amplification of the signal. In particular, the induced ellipticity benefits from the geometric mean field $\sqrt{E_a E_{\rm probe}}$, effectively boosting the axion signal strength. This hybrid approach allows the experiment to surpass the traditional quantum shot-noise limit associated with laser light. As shown in Fig. 2 of Ref. [90], the injection of probe photons significantly enhances the SNR when the laser shot noise exceeds the sampling rate, corresponding to regions II and III in the figure. In contrast, when the shot noise is lower than the sampling rate (regions I and IV), the addition of probing power leads to reduced SNR due to unnecessary variance amplification in the electro-optic signal readout.

Owing to the resulting enhancement in SNR—by several orders of magnitude—this method offers considerable flexibility in experimental design. For example, one can reduce the laser power from 10 to 1 mW while maintaining sensitivity to axions with DFSZ-level coupling. Future developments could include spatially optimized EO geometries and dynamic modulation of the probe signal to further suppress noise and improve detection fidelity. Since the axion-probe beat signal appears at low frequencies (typically 1–50 kHz), laser phase noise is not a limiting factor, provided a low-noise narrow-linewidth laser is used. Locking the laser to a Fabry-Pérot cavity further suppresses phase fluctuations in this band. While probing techniques can, in principle, introduce their own quantum limits, in the present optical readout scheme such effects are not expected to pose a significant limitation. The dominant quantum noise source remains the vacuum fluctuations of the resonant cavity field. Since the injected rf probe is a coherent classical signal and the detection process involves measuring optical ellipticity rather than amplifying the microwave field, any additional quantum noise introduced by probing is expected to lie below the vacuum noise floor. As such, the overall sensitivity is ultimately limited by the cavity's zero-point fluctuations, which are already accounted for in our analysis.

Until practical single-photon detectors become available in the gigahertz regime [98–105], the method presented here offers a compelling enhancement in both sensitivity and scanning speed. Specifically, this approach can accelerate axion searches by more than an order of magnitude through two mechanisms. First, by injecting a coherent probe tone and detecting the axion-induced beat signal via an EO crystal, the effective SNR exceeds the noise limit of conventional haloscopes by a factor of 5–10 [17,19,28,33–35,37–39,42,46,50,67,74,85,106–110]. Since the scanning rate scales inversely with the square of the SNR, this corresponds to a 25–100× increase in scanning speed while still achieving DFSZ sensitivity, even with the modest integration time of 3 s per frequency step assumed throughout this work. Second, the same Fabry-Pérot laser readout system can be used uniformly across a wide frequency range—from 0.5 to at least 50 GHz—without reconfiguring the detection chain. This broadband capability is a critical advantage over conventional linear amplifiers and quantum-limited photon counters, which typically require frequency-specific optimization. Together, these features make the present method a versatile and powerful strategy for exploring the high-frequency axion parameter space that remains largely open. For more discussion on this subject, see Appendix C.

A. Leveraging axion spatial coherence

An immediate and practical extension of the present method would be to deploy a modest array of probing haloscopes operating in parallel. Given that vacuum fluctuations are uncorrelated between separate cavities, while the axion field remains spatially coherent over macroscopic

scales, coherently combining the outputs of N detectors leads to a signal that scales as N, while the noise grows only as $\sqrt{N}$. Thus, the overall signal-to-noise ratio improves as

$$\mathrm{SNR}_{\mathrm{total}} \propto \frac{N}{\sqrt{N}} = \sqrt{N},$$

for fixed total integration time, equivalent to a single search with a volume NV.

This strategy is justified by the fact that the axion field is expected to behave as a classical, spatially coherent oscillation over a characteristic coherence length

$$\ell_{\mathrm{coh}} \sim \frac{2\pi}{m_a v} \sim 100 \text{ m to } 1 \text{ km}, \tag{30}$$

depending on the axion mass m_a (or frequency ν_a) and its virial velocity $v \sim 10^{-3}$. For example, at $\nu_a = 1$ GHz, the coherence length is approximately 200 m, ensuring that ten or more detectors within this radius observe the same axion phase and can be summed coherently.

The distinction between coherent axion signal and incoherent quantum or thermal noise is especially important when targeting higher-frequency axions. In that regime, the resonant cavity volume must shrink to maintain the desired frequency, limiting the available signal power. One can compensate for the loss of volume by launching several experiments in parallel, tuned at the same frequency. Since the optical Fabry-Pérot readout system is compact, stable, and easily replicated, a tenfold array is straightforward to implement with current technology and could provide the required improvement in sensitivity or scanning rate—without introducing additional quantum or thermal noise limitations.

B. Implications for axion haloscopes

We note that the EO-based electric field readout method, especially when combined with probing, could offer significant advantages to other haloscope-style axion experiments, such as, e.g., ADMX, MADMAX, and ALPHA.

In MADMAX, the dielectric disk configuration enhances axion-photon conversion but currently requires extremely low noise power detection. Incorporating EO-based field readout could allow detection of the same signal with reduced thermal and quantum noise concerns, potentially allowing operation at 1 K or even higher.

The ALPHA experiment also operates at higher frequencies in compact resonators and faces similar challenges from quantum noise and dilution refrigeration complexity. Because EO readout responds to electric field amplitude rather than energy, it provides a more favorable SNR scaling and offers a path forward for simplified cryogenic operation. A key advantage of the proposed approach is the elimination of readout noise as a limiting factor in axion detection. By replacing conventional rf amplification chains with an optical probing system using a coherent laser and Fabry-Pérot interferometry, we suppress the dominant quantum and thermal noise sources that typically constrain integration times. This unlocks significantly faster scanning rates and ensures sensitivity to axion signals across a wide frequency range—independent of the electronic noise floor that currently limits haloscope performance.

Together, these implications suggest that EO-based probing methods represent a compelling new detection paradigm for future axion searches.

IV. CONCLUDING REMARKS AND SUMMARY

The CARAMEL method proposed in this work achieves a decisive advantage by replacing quantum-limited microwave amplification with a low-noise optical readout, even though the axion-photon conversion mechanism and the resonator design are conceptually identical to those used in traditional haloscope experiments. This readout scheme leverages the EO effect to convert weak electric field modulations into laser polarization signals, which can be measured with shot-noise-limited sensitivity over narrow detection bandwidths. In doing so, CARAMEL retains all the standard haloscope principles while extending their reach through a fundamentally different detection chain.

In addition to its low-noise readout advantage, CARAMEL offers two notable system-level benefits. First, it enables a unified detection platform across a vast frequency range, from subgigahertz to tens of gigahertz, without the need for reconfiguring quantum-limited amplifiers or microwave components. Second, it eliminates the added noise introduced by microwave amplification, which—even at the quantum limit—contributes at least half a photon of noise power to the system. The optical readout scheme in CARAMEL bypasses this fundamental amplifier constraint, allowing high-sensitivity measurements without incurring quantum-limited amplification penalties. We note that the CARAMEL approach does not beat vacuum noise in the absolute sense, but it resolves an axion signal in a narrow bin where vacuum noise is statistically small. This is achieved through the combined use of probing, Fabry-Pérot enhancement, and long integration. Thus, our method does not eliminate vacuum fluctuations—it resolves the axion field against them using time and coherence. We emphasize that the EO or FP stage serves as an optical field amplifier, not a resonant element at the axion frequency. As a result, the axion search bandwidth is determined solely by the microwave cavity and the bandwidth of the optical detection chain rather than by the Fabry-Pérot resonator.

In summary, CARAMEL unifies optical and rf techniques to achieve axion dark matter detection with enhanced sensitivity beyond the quantum noise limit. Its ability to operate across a broad frequency range, with low optical power and without complex quantum amplifiers, opens a scalable path forward in the high-frequency regime. Our approach is complementary to existing axion haloscopes

and provides a versatile platform for future axion dark matter searches. The method described in this work is projected to cover much—perhaps all [16]—of the relevant parameter space for postinflationary axion dark matter and may lead to a breakthrough in resolving puzzles regarding both the subatomic interactions of hadrons and the large-scale structure of the Universe.

ACKNOWLEDGMENTS

The work of H. D. is supported by the U.S. Department of Energy under Grant Contract No. DE-SC0012704. Y. K. S. is indebted to KAIST and, in particular, to the Physics Department for support to finish this work. Y. K. S. acknowledges fruitful discussions with Junu Jeong on the impact of zero-point fluctuations on the signal-to-noise ratio in single- versus multiple-cavity configurations.

DATA AVAILABILITY

No data were created or analyzed in this study.

APPENDIX A: LASER SIGNAL-TO-NOISE RATIO ESTIMATION

We estimate the SNR for the axion-induced ellipticity in the probing method with optical readout.

The shot-noise-limited ellipticity sensitivity of the laser readout system is given by

$$\delta\psi_{\rm shot} = \sqrt{\frac{2h\nu}{P}} \approx 6.1\ \text{nrad}/\sqrt{\text{Hz}}, \tag{A1}$$

where $\nu \approx 2.82 \times 10^{14}$ Hz is the laser frequency and $P = 10$ mW the laser power.

The axion-induced ellipticity is enhanced by the externally injected rf probing field and the finesse of the optical cavity. For the chosen parameters of FP finesse of 10^4 and rf probing power of 2 nW, the expected signal amplitude is

$$\psi_a \approx 490\ \text{nrad}. \tag{A2}$$

The axion field has a finite coherence time of approximately

$$\tau_a = \frac{1}{\Delta\nu_a} \approx 100\ \mu\text{s}, \tag{A3}$$

corresponding to a bandwidth of $\Delta\nu_a = 10$ kHz. During a total integration time $t = 3$ s, the number of independent coherence segments is

$$N = \frac{t}{\tau_a} = t \cdot \Delta\nu_a = 3\ \text{s} \times 10^4\ \text{Hz} = 3 \times 10^4. \tag{A4}$$

The shot noise within each coherence time is

$$\delta\psi_{\rm seg} = \delta\psi_{\rm shot} \cdot \sqrt{\Delta\nu_a} = 6.1\ \text{nrad} \cdot 100 = 610\ \text{nrad}. \tag{A5}$$

Averaging incoherently over N segments, the total noise decreases as

$$\delta\psi = \frac{610\ \text{nrad}}{\sqrt{3 \times 10^4}} \approx 3.5\ \text{nrad}. \tag{A6}$$

Therefore, the final SNR is given by

$$\text{SNR} = \frac{\psi_a}{\delta\psi} = \frac{490\ \text{nrad}}{3.5\ \text{nrad}} \approx 140. \tag{A7}$$

This confirms that the probing method with optical readout can detect the axion-induced signal at high significance within a short integration time, provided the axion frequency is on resonance.

APPENDIX B: SIGNAL-TO-NOISE RATIO DEPENDENCE ON QUALITY FACTOR AND TEMPERATURE

Here, we clarify the proper use of thermal noise field expressions and demonstrate how the probing method automatically reduces the thermal noise and improves the SNR, especially when the cavity quality factor is lower than the axion coherence quality factor, $Q_c \ll Q_a$. The same effect can be achieved by effectively integrating over the axion bandwidth.

1. Thermal noise in a resonant cavity mode

For a single resonant mode at angular frequency $\omega = 2\pi\nu$, the average thermal energy in the mode is

$$U_{\rm mode} = \left(\bar{n}_{\rm th} + \frac{1}{2}\right)\hbar\omega, \tag{B1}$$

where $\bar{n}_{\rm th} = 1/(e^{\hbar\omega/k_BT} - 1)$ is the thermal occupation number.

This energy is shared equally between the electric and magnetic fields. The electric field rms amplitude is, therefore,

$$E_{\rm th}^{(\rm mode)} = \sqrt{\frac{(\bar{n}_{\rm th} + \frac{1}{2})\hbar\omega}{\epsilon_0 V}}, \tag{B2}$$

where V is the effective mode volume. In a more compact form, $U_{\rm mode} = \frac{\hbar\omega}{2}\coth(\frac{\hbar\omega}{2k_BT})$, and so

$$E_{\rm th}^{(\rm mode)} = \sqrt{\frac{\hbar\omega\,\coth(\frac{\hbar\omega}{2k_BT})}{2\epsilon_0 V}}, \tag{B3}$$

which is valid in both the classical and quantum limit.

2. Thermal noise in a band-limited measurement

In the classical limit, the thermal noise has a flat power spectral density near gigahertz frequencies, given by

$$dP_{\rm noise}/d\nu = k_BT[\rm W/Hz]. \tag{B4}$$

When a detector samples a bandwidth $\Delta\nu$ for a time Δt, the total thermal energy collected is

$$U = k_BT\cdot\Delta\nu\cdot\Delta t. \tag{B5}$$

Assuming half of this energy contributes to the electric field and half to the magnetic field [97], the corresponding rms electric field amplitude is

$$E_{\rm th}^{(\rm probe)} = \sqrt{\frac{k_BT\cdot\Delta\nu\cdot\Delta t}{\epsilon_0 V}}. \tag{B6}$$

Let us introduce the reduced quality factor $Q_{\rm red} = Q_aQ_c/(Q_a+Q_c)$, which we will use below.

3. The effect of probing on SNR in the low-quality factor regime

In the regime $Q_c \ll Q_a$, the axion signal is spectrally narrow ($\Delta\nu_a = \omega/2\pi Q_a$), but the cavity bandwidth $\Delta\nu_c = \omega/2\pi Q_c$ is broad. This mismatch would ordinarily result in collecting excess thermal noise.

However, the probing method changes this: A narrow-band probe tone is injected at frequency ω_p near the axion frequency ω_a, and the detection system is sensitive only to the interference between the axion field and the probe. This effectively limits the measurement bandwidth to $\Delta\nu = \omega/(2\pi Q_a)$, matching the axion coherence bandwidth. Since the axion field is coherent over a time $\tau_a = Q_a/\nu$ [more accurately, $\tau_{\rm coherence} = (Q_a+Q_c)/\nu$, but we will use the above definition for simplicity when $Q_c \ll Q_a$], the measurement remains Fourier limited with $\Delta\nu\cdot\tau_a = 1$. The same effect is obtained by integrating the signal only over the axion bandwidth. If this is not possible, the probing can be used to achieve the narrow filtering automatically.

Although the cavity supports thermal noise across its full bandwidth, only thermal fluctuations within the narrow axion bandwidth contribute to the detected beat signal. This acts as an effective filtering mechanism, and the resulting thermal noise field is reduced by a factor $\sqrt{Q_c/Q_a}$ compared to the full cavity thermal field:

$$E_{\rm th}^{(\rm probe)} = \sqrt{\frac{k_BT}{\epsilon_0 V}}\cdot\sqrt{\frac{Q_c}{Q_a}}. \tag{B7}$$

More generally, the reduction is equal to $\sqrt{(Q_{\rm red}/Q_a)}$:

$$E_{\rm th}^{(\rm probe)} = \sqrt{\frac{k_BTQ_{\rm red}}{\epsilon_0 VQ_a}}. \tag{B8}$$

The axion to photon conversion power scales as $P_a = P_0[(Q_cQ_a)/(Q_c+Q_a)] = P_0Q_{\rm red}$, with $P_0 = 10^{-23}$ W/10[4]. The axion-induced field becomes

$$E_a = \sqrt{\frac{P_0Q_{\rm red}Q_c}{\epsilon_0 V\omega}}. \tag{B9}$$

The resulting SNR is

$$\mathrm{SNR}(t) = \frac{E_a}{E_{\rm th}^{(\rm probe)}}\cdot\sqrt{\frac{t}{\tau_a}} = \sqrt{\frac{P_0Q_ct}{2\pi k_BT}}. \tag{B10}$$

The integrated SNR over time t is proportional to $\sqrt{Q_ct/T}$ and independent of the axion Q_a. The more general equation is given by

$$\mathrm{SNR}(t) = \frac{E_a}{E_{\rm th}^{(\rm probe)}}\cdot\sqrt{\frac{t}{\tau_a}} = \sqrt{\frac{P_0Q_{\rm red}t}{2\pi k_BT}}, \tag{B11}$$

which reduces to Eq. (B10) above when the cavity quality factor $Q_c \ll Q_a$.

4. The effect of cavity narrowness on SNR in the high-quality factor regime

When $Q_c \gg Q_a$, the cavity is narrower than the axion linewidth. The axion power saturates:

$$P_a \approx P_0Q_a, \tag{B12}$$

and the axion-induced electric field amplitude becomes

$$E_a = \sqrt{\frac{P_0Q_aQ_c}{\epsilon_0 V\omega}}, \tag{B13}$$

while the thermal noise field

$$E_{\rm th} = \sqrt{\frac{k_BT}{\epsilon_0 V}}. \tag{B14}$$

Using $\tau_{\rm coherence} = (Q_c+Q_a)/\nu \approx Q_c/\nu$, the SNR becomes

$$\mathrm{SNR}(t) = \frac{E_a}{E_{\mathrm{th}}} \cdot \sqrt{\frac{t}{\tau_{\mathrm{coherence}}}} = \sqrt{\frac{P_0 Q_a t}{2\pi k_B T}}, \tag{B15}$$

which can also result from Eq. (B11) above for $Q_c \gg Q_a$. The integrated SNR is now proportional to $\sqrt{Q_a t/T}$ and independent of the cavity Q_c. The SNR scaling as $\sqrt{Q_c}$ holds only when $Q_c \lesssim Q_a$. For $Q_c \gg Q_a$, two competing effects emerge: While the cavity field amplitude continues to increase with Q_c, so does the thermal noise field, since the narrower cavity mode enhances thermal fluctuations per unit bandwidth despite admitting less total bandwidth. Simultaneously, only a fraction Q_a/Q_c of the axion power spectrally overlaps with the cavity mode. These effects combine to cancel any further SNR gain, leading to saturation as Q_c increases. The optimal regime is, therefore, $Q_c \approx Q_a$, where both the axion power and the thermal noise are spectrally matched. Future advances in single-photon detectors will be critical for pushing axion sensitivity further, particularly at low temperatures since they do not suffer from limitations due to zero-point fluctuations [98–105].

5. General SNR expression including quantum fluctuations

Using Eq. (B3) and a procedure similarly as above, the thermal noise within the relevant band width is

$$E_{\mathrm{th}}^{(\mathrm{probe})} = \sqrt{\frac{\hbar\omega \coth(\frac{\hbar\omega}{2k_B T}) Q_{\mathrm{red}}}{2\epsilon_0 V Q_a}}. \tag{B16}$$

This allows one to define the SNR as

$$\mathrm{SNR}(t) = \frac{E_a}{E_{\mathrm{th}}^{\mathrm{probe}}} \cdot \sqrt{\frac{t}{\tau_{\mathrm{coherence}}}} = \sqrt{\frac{P_0 Q_{\mathrm{red}} t}{\pi\hbar\omega \coth(\frac{\hbar\omega}{2k_B T})}}, \tag{B17}$$

which is the most general equation valid in both the classical ($k_B T \gg \hbar\omega$) and quantum ($k_B T \ll \hbar\omega$) regimes and all values of the cavity quality factors. For completeness, in the quantum limit, the SNR becomes

$$\mathrm{SNR}(t) = \frac{E_a}{E_{\mathrm{th}}} \cdot \sqrt{\frac{t}{\tau_{\mathrm{coherence}}}} = \sqrt{\frac{P_0 Q_{\mathrm{red}} t}{\pi\hbar\omega}}. \tag{B18}$$

Thus, by using probing to reduce thermal noise and understanding the interplay with vacuum fluctuations, one can access high-SNR regimes even when the cavity quality factor is not ideally matched to the axion coherence.

The SNR scales as $1/\sqrt{T}$ and benefits from $\sqrt{Q_c}$ up to the axion quality factor Q_a. In the quantum regime, SNR is leveled off at low temperatures and it improves with increasing $\sqrt{Q_c}$, again up to the axion quality factor. Figure 3 shows that it is possible to overcome the thermal noise background by employing a combination of low temperature and high cavity quality factor.

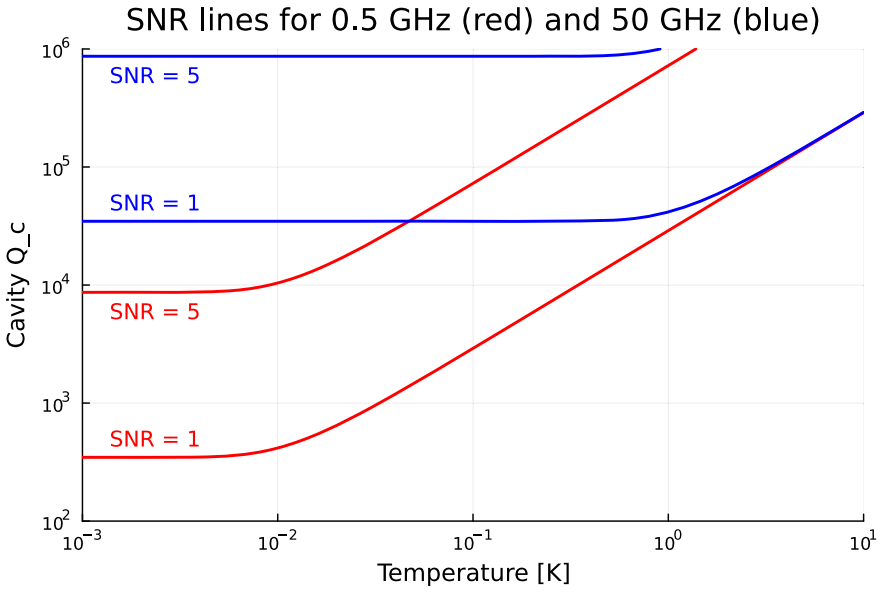


FIG. 3. SNR as a function of Q_c and T at different operating frequencies. The transition from the quantum regime to the classical regime becomes apparent around 24 mK for 0.5 GHz (red) and 2.4 K for 50 GHz (blue), where the thermal photon occupation number begins to exceed the vacuum (zero-point) contribution. The cavity volume is kept constant at 3.7 liters. The axion to photon conversion power is kept at 10^{-23} W assuming $Q_c = 10^4$ and scaled appropriately for different cavity quality factor values; see the text.

APPENDIX C: BANDWIDTH CONSIDERATIONS VIA RF PROBING IN EO AXION DETECTION

In the EO probing method for axion dark matter detection, the injection of a coherent rf tone into the cavity radically alters the nature of the signal readout. Most importantly, it enables a dramatic reduction of the effective detection bandwidth, directly improving the SNR and enabling sensitivity beyond the conventional quantum limit associated with microwave amplifiers. However, the zero-point fluctuations of the electromagnetic field (vacuum noise) inside the cavity still remain.

1. Principle of rf probing

In traditional haloscope experiments, the axion-induced signal appears as a weak oscillating electric field with a narrow intrinsic bandwidth determined by the velocity dispersion of the dark matter halo:

$$\Delta\nu_a = \frac{\nu_a}{Q_a} \sim 10^{-6}\nu_a \sim 10\ \text{kHz}, \tag{C1}$$

for axion frequencies $\sim$10 GHz.

Without rf probing, one must integrate over this full axion bandwidth to recover the signal power, with noise accumulating over the same bandwidth.

By injecting a coherent rf tone $E_p \cos(\omega_p t)$ near the expected axion frequency ω_a, the axion field $E_a \cos(\omega_a t + \phi(t))$ interferes with it to generate a beat signal at the difference frequency:

$$\omega_b = |\omega_a - \omega_p| \sim \text{few kHz}. \tag{C2}$$

This beat modulates the birefringence of the EO crystal and appears as a low-frequency modulation in the polarization of a transmitted laser beam.

2. Detection bandwidth from integration time

The probing technique concentrates the axion-induced signal into a narrow spectral line. The detection bandwidth is not set by $\Delta\nu_a$ but by the inverse of the integration time:

$$\Delta\nu_{\text{det}} = \frac{1}{t}. \tag{C3}$$

For $t = 3$ s, $\Delta\nu_{\text{det}} \sim 0.33$ Hz. This allows one to measure a variance signal in a very narrow frequency bin, thereby reducing noise contribution.

3. Vacuum noise is present and probed

Vacuum fluctuations in the cavity, with rms field

$$E_{\text{vac}} = \sqrt{\frac{\hbar\omega}{2\epsilon_0 V}}, \tag{C4}$$

are broadband and random phase. When a coherent probe field is injected, vacuum noise beats with it just like the axion field does:

$$E(t) = E_{\text{probe}} \cos(\omega t) + \delta E(t), \tag{C5}$$

with $\delta E(t)$ including vacuum, thermal, and axion components.

The ellipticity is proportional to

$$\psi(t) \propto E(t)^2 \propto 2E_{\text{probe}}\delta E(t), \tag{C6}$$

which includes vacuum-induced and axion-induced modulation.

Therefore, the EO method does *not eliminate* vacuum noise—it still contributes to the measured ellipticity fluctuations.

4. Why CARAMEL can still resolve the axion

What CARAMEL does is leverage:

(i) coherent rf probing to up-convert the axion signal into a narrow beat note;
(ii) Fabry-Pérot enhancement to increase signal ellipticity;
(iii) narrow-band optical readout $\Delta\nu_{\text{det}} \ll \Delta\nu_a \leq \Delta\nu_{\text{cav}}$ to suppress broadband noise.

Therefore, although the axion field is weaker than the vacuum field (e.g., $E_a/E_{\text{vac}} \sim 10^{-2} - 10^{-1}$) it is concentrated in a single narrow bin, while the vacuum noise is spread across $\Delta\nu \sim \nu/Q_c$. The effective vacuum noise in the detection bin is

$$E_{\text{vac,eff}} = E_{\text{vac}} \cdot \sqrt{\frac{\Delta f_{\text{det}}}{\Delta f_{\text{cavity}}}}, \tag{C7}$$

which can be $\sim 10^2 - 10^3$ times smaller than the total rms vacuum field.

APPENDIX D: FEASIBILITY OF THE QUANTUM READOUT SYSTEM (QRS)

This appendix summarizes feasibility in three parts: (i) thermal loading *vs.* QRS location, (ii) sensitivity and demodulation (showing explicitly why no "washout" occurs), and (iii) EO-crystal length and probing-power scaling with axion frequency. Throughout, we reference the schematic in Fig. 4.

The key parameters of the EO or FP (QRS) readout have been verified to be mutually consistent across the expected operating range. At 10 GHz the signal from the microwave cavity is mixed down to $\sim$10 kHz, while at 50 GHz it is demodulated to $\sim$50 kHz; the 10–50 kHz frequencies are orders of magnitude smaller than any relevant optical bandwidth in the Fabry-Pérot cavity, ensuring that the polarization modulation is not averaged out.

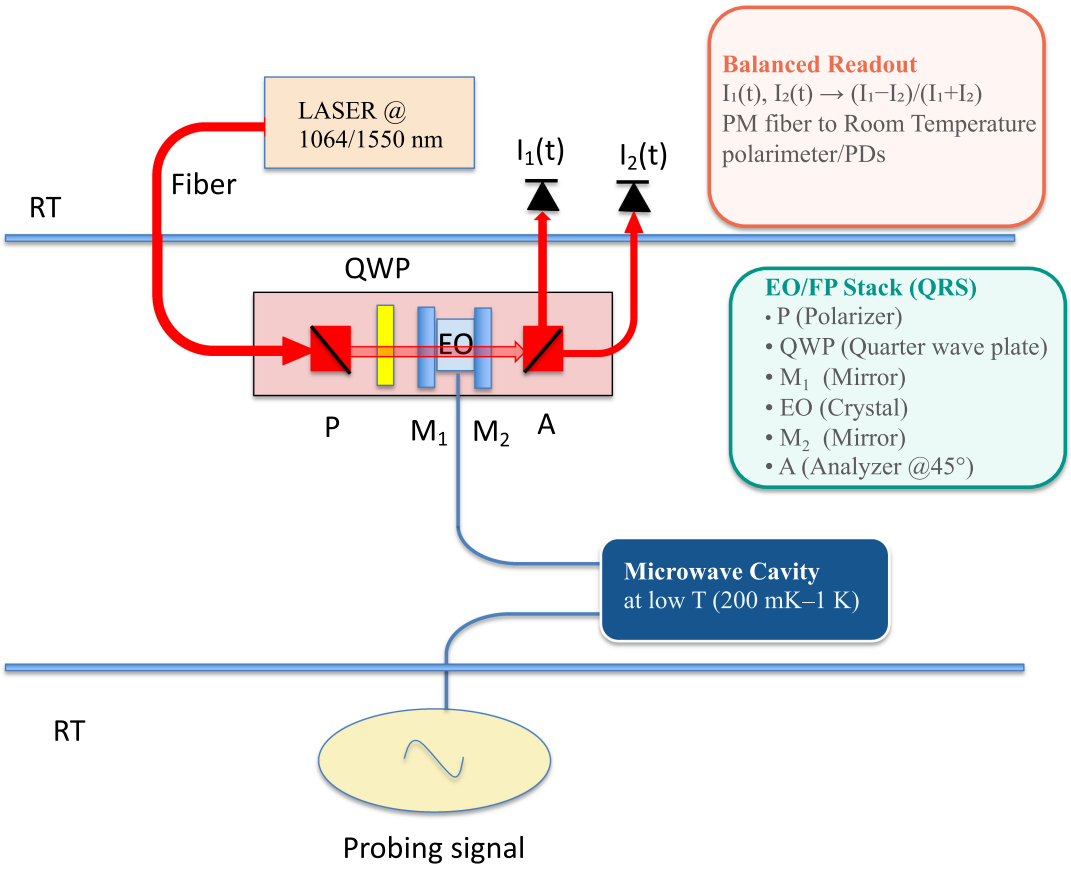


FIG. 4. Schematic of the QRS used in the feasibility analysis. The microwave cavity is placed at the lowest required operating temperature (typically 0.2–1 K depending on the target frequency), while the QRS is mounted on the top plate and coupled to the cavity via a short, impedance-matched rf cable. The EO crystal is embedded between two high-reflectivity mirrors that form the Fabry-Pérot resonator and is probed by a linearly polarized laser. A polarizer, quarter-wave plate (QWP), and analyzer (oriented at 45° relative to the polarizer) convert the axion-induced ellipticity modulation into a detectable polarization rotation. The resulting signal is read out using balanced photodiodes (PDs) at room temperature (RT), which measure the normalized differential output $(I_1(t) - I_2(t))/(I_1(t) + I_2(t))$. Since the required cavity temperatures do not need to fall below 0.2–1 K across the targeted frequency range, the laser-induced absorption in the EO crystal must remain below ∼10% of the available cooling power at that temperature. Depending on the available laboratory infrastructure, the EO or FP stage may alternatively be positioned at the 4 K plate, remaining electrically coupled to the cavity while being only weakly thermally anchored to it.

Because the optical absorption coefficient of $LiNbO_3$ is too large to sustain milliwatt-scale laser powers at high finesse, the allowable laser intensity inside the dilution refrigerator is set by the cryogenic thermal budget rather than by optical considerations. For $\mathcal{F} = 10^4$ and a 3 mm EO crystal, the measured absorption corresponds to an absorbed power $P_{\rm abs} \simeq 0.13 P_\ell$, where P_ℓ is the incident laser power. Imposing a conservative thermal limit $P_{\rm tot} = P_{\rm abs} + P_{\rm rf} \leq 5\ \mu$W and allowing up to $P_{\rm rf} = 2\ \mu$W of coherent probe power yields $P_\ell \lesssim 23\ \mu$W. This operating point restores the full $\mathcal{F} = 10^4$ FP enhancement while remaining safely within the cryogenic load budget. At such low optical powers, laser shot noise is negligible compared to the variance feature generated by axion-probe interference.

The FP resonator, filled by a $LiNbO_3$ crystal of refractive index $n \simeq 2.2$ at 1064 nm, has a free-spectral range (FSR)

$$\mathrm{FSR} = \frac{c}{2nL_{\rm FP}}, \qquad \Delta\nu_{\rm FP} = \frac{\mathrm{FSR}}{\mathcal{F}}. \tag{D1}$$

For a $L_{\rm FP} = 3$ mm (assumed equal to the crystal length L_c) and $\mathcal{F} = 10^4$, one obtains FSR ≈ 22.7 GHz and a linewidth $\Delta\nu_{\rm FP} = 2.3$ MHz, comfortably larger than the modulation frequencies (10–50 kHz). The EO modulation, therefore, lies fully within the same FP resonance, guaranteeing faithful transmission of the sidebands and preserving the ellipticity-variance measurement.

To maintain a large enough signal-to-noise ratio as the target frequency increases, the EO-crystal length can be reduced in proportion to the axion frequency (e.g., L_c: 3 mm → 0.6 mm for 10 → 50 GHz) while the microwave probe power $P_{\rm rf}$ can be raised to compensate for it. The shorter crystal reduces optical absorption and allows

higher circulating optical power, while the higher $P_{\rm rf}$ compensates for the smaller EO-interaction volume. Under these conditions the demodulated signal bandwidth (10–50 kHz) remains far below $\Delta\nu_{\rm FP}$, confirming that all parameter combinations discussed are thermally and dynamically feasible.

1. Thermal location and loading

The thermal feasibility of the QRS depends primarily on the absorbed optical power:

$$P_{\rm abs} = \alpha L_c \frac{\mathcal{F}}{\pi} P_\ell, \tag{D2}$$

where α is the absorption coefficient of the EO crystal, L_c its optical length, $\mathcal{F}$ the finesse of the FP cavity, and P_ℓ the incident laser power. For $LiNbO_3$ at 1064 nm, $\alpha \simeq (3-5)\times 10^{-3}$ cm^{-1} at room temperature and decreases by roughly one order of magnitude at cryogenic temperatures.

Using $L_c = 3$ mm, a finesse of 10^4, and $P_\ell = 0.1$ mW gives

$$P_{\rm abs} \approx (4\times 10^{-3}\times 0.3)\frac{\mathcal{F}}{\pi} P_\ell \simeq 0.13 \times P_\ell \approx 13\ \mu{\rm W}, \tag{D3}$$

which remains well below the available cooling power of typical dilution refrigerators at 0.2–1 K. Had the original $P_\ell = 10$ mW been retained, the absorbed power would increase by 2 orders of magnitude, clearly exceeding the 0.2 K cooling capability but not at 1 K. Thus, lowering the laser power to $P_\ell \sim 0.1$ mW alone suffices to make the system thermally viable while keeping the SNR very high.

Consequently, the QRS can safely be located either directly on top of the cavity—thermalized at the same stage as the resonator—or at the 4 K plate, depending on the target axion frequency. For operation below ~15 GHz, the cavity typically resides near 0.1–0.2 K and the QRS can be comounted on its top plate without imposing a thermal load greater than $\leq$10% of the available cooling power. At higher frequencies (e.g., 50 GHz), the signal-to-noise ratio saturates already near 1 K, where the available cooling power is larger by T^2 more than one order of magnitude, permitting optical powers up to the milliwatt level without penalty.

The microwave coupling between the cavity and QRS is realized through a short, thermally anchored coaxial line (typically ~10 cm). Since the injected rf power is only in the range of 200 nW − 1 μW, the corresponding Joule dissipation in the coupling network remains negligible compared with the cooling power at all stages.

2. Demodulated (variance) sensitivity

In the probing scheme, the EO or FP stage converts the axion-driven cavity field into a polarization signal whose *mean* is time independent, while its *variance* fluctuates on the axion coherence timescale. The relevant frequency scale is set solely by the axion coherence bandwidth

$$\Delta\nu_a \simeq \nu_a (v/c)^2,$$

with $v \approx 10^{-3}c$, which gives $\Delta\nu_a \sim 10$ kHz at $\nu_a =$ 10 GHz and ~50 kHz at $\nu_a = 50$ GHz. The power spectral density of the ellipticity (or differential intensity), therefore, exhibits a narrow feature of width $\Delta\nu_a$ around the baseband. We sample at $\nu_s \gg 2\Delta\nu_a$ and estimate the variance within a window $B \sim \Delta\nu_a$ (or, equivalently, $B \sim 1/t$ for matched integration).

The SNR of the variance estimate follows the radiometer law for power detection:

$$\mathrm{SNR} = \frac{P_s}{k_B T_n}\sqrt{\frac{t}{B}},$$

where P_s is the power in the variance feature, T_n the equivalent noise temperature, t the integration time, and B the analysis bandwidth. For $t \leq \tau_c$ (with $\tau_c \sim 1/\pi\Delta\nu_a$), matched filtering implies $B \sim 1/t$ and, hence, SNR $\propto t$. For $t \gg \tau_c$, the data contain $N = t/\tau_c$ statistically independent coherence segments, and the optimal estimator's variance decreases as $1/\sqrt{N}$, yielding the familiar

$$\mathrm{SNR} \propto \sqrt{t/\tau_c}.$$

This is the same long-time $t^{1/2}$ scaling used in phase-preserving haloscope analyses; here, it applies to the variance feature centered at baseband with width Δf_a.

3. Frequency-crystal-power scaling

Because the microwave cavity and its stored field remain constant, maintaining the same SNR across the 10–50 GHz range requires only modest adjustments in the EO parameters. Shortening the EO crystal at higher frequencies increases the FSR. At the same time, the microwave probe power can be increased within the same cavity coupling configuration to compensate for the smaller EO interaction length, preserving the effective modulation depth. Because the absorbed optical load remains fixed by a ≤ 5 μW budget at the low frequencies (around 1 GHz), the allowable laser power scales weakly with L_c, and the system maintains nearly constant SNR (SNR ≈ 38 at $t = 3$ s) over the full frequency span. Representative parameter choices consistent with the thermal and optical constraints are summarized in Table II. The parameter values listed in Table I are

TABLE II. Representative QRS parameters as a function of frequency, assuming fixed cavity volume and a total thermal load ≤ 5 μW. The operating point maintains $\mathcal{F} = 10^4$ across the full band.

Parameter	10 GHz	30 GHz	50 GHz
T_{cav} (K)	0.2	0.5	1.0
L_c (mm)	3.0	1.5	0.6
$\mathcal{F}$	10^4	10^4	10^4
P_ℓ (μW)	23	23	23
P_{RF} (μW)	2.0	2.0	2.0
FSR (GHz)	22.7	68	113
$\Delta\nu_{\mathrm{FP}}$ (MHz)	2.27	6.8	11.3
f_{mod} (kHz)	10	30	50
SNR (3 s)	∼38	∼38	∼38

feasible as long as the QRS is mounted at the 4 K plate of the dilution refrigerator, where the cooling power is adequate.

This scaling shows that as the frequency increases, the EO crystal becomes shorter and optically more efficient, while the broadened FSR and available probe power ensure that both the thermal and dynamic conditions remain easily satisfied.

Implementation note. If thermal budget on the coldest stage is tight, one could place the QRS on the 4 K plate and couple the cavity to the EO capacitor via a short, impedance-matched line with *in situ* attenuation mounted at the cavity temperature so that the cavity does not see 4 K noise. The optical readout remains unchanged; the demodulated signal at ∼10 kHz is unaffected, and the FP still satisfies $f_{\mathrm{mod}} \ll \Delta\nu_{\mathrm{FP}}$.

[1] S. Weinberg, A new light boson?, Phys. Rev. Lett. **40**, 223 (1978).
[2] F. Wilczek, Problem of strong P and T invariance in the presence of instantons, Phys. Rev. Lett. **40**, 279 (1978).
[3] R. D. Peccei and H. R. Quinn, *CP* conservation in the presence of instantons, Phys. Rev. Lett. **38**, 1440 (1977).
[4] R. D. Peccei and H. R. Quinn, Constraints imposed by *CP* conservation in the presence of instantons, Phys. Rev. D **16**, 1791 (1977).
[5] J. Preskill, M. B. Wise, and F. Wilczek, Cosmology of the invisible axion, Phys. Lett. **120B**, 127 (1983).
[6] P. Sikivie, Experimental tests of the "invisible" axion, Phys. Rev. Lett. **51**, 1415 (1983).
[7] M. Dine, W. Fischler, and M. Srednicki, A simple solution to the strong *CP* problem with a harmless axion, Phys. Lett. B **104**, 199 (1981).
[8] D. E. Kaplan, T. Melia, and S. Rajendran, What can solve the strong *CP* problem?, J. High Energy Phys. 08 (2025) 050.
[9] D. J. E. Marsh, Axion cosmology, Phys. Rep. **643**, 1 (2016).
[10] E. Berkowitz, M. I. Buchoff, and E. Rinaldi, Lattice QCD input for axion cosmology, Phys. Rev. D **92**, 034507 (2015).
[11] G. Ballesteros, J. Redondo, A. Ringwald, and C. Tamarit, Unifying inflation with the axion, dark matter, baryogenesis and the seesaw mechanism, Phys. Rev. Lett. **118**, 071802 (2017).
[12] S. Borsanyi *et al.*, Calculation of the axion mass based on high-temperature lattice quantum chromodynamics, Nature (London) **539**, 69 (2016).
[13] M. Dine, P. Draper, L. Stephenson-Haskins, and D. Xu, Axions, instantons, and the lattice, Phys. Rev. D **96**, 095001 (2017).
[14] V. B. Klaer and G. D. Moore, The dark-matter axion mass, J. Cosmol. Astropart. Phys. 11 (2017) 049.
[15] M. Buschmann, J. W. Foster, and B. R. Safdi, Early-universe simulations of the cosmological axion, Phys. Rev. Lett. **124**, 161103 (2020).
[16] M. Buschmann, J. W. Foster, A. Hook, A. Peterson, D. E. Willcox, W. Zhang, and B. R. Safdi, Dark matter from axion strings with adaptive mesh refinement, Nat. Commun. **13**, 1049 (2022).
[17] N. Du *et al.* (ADMX Collaboration), A search for invisible axion dark matter with the axion dark matter experiment, Phys. Rev. Lett. **120**, 151301 (2018).
[18] C. Bartram *et al.* (ADMX Collaboration), Axion dark matter experiment: Run 1B analysis details, Phys. Rev. D **103**, 032002 (2021).
[19] C. Bartram *et al.* (ADMX Collaboration), Search for invisible axion dark matter in the $3.3 - 4.2$ μeV mass range, Phys. Rev. Lett. **127**, 261803 (2021).
[20] C. Boutan *et al.* (ADMX Collaboration), Axion dark matter experiment: Run 1A analysis details, Phys. Rev. D **109**, 012009 (2024).
[21] C. Goodman *et al.* (ADMX Collaboration), ADMX axion dark matter bounds around 3.3 μeV with Dine-Fischler-Srednicki-Zhitnitsky discovery ability, Phys. Rev. Lett. **134**, 111002 (2025).
[22] G. Carosi *et al.* (ADMX Collaboration), Search for axion dark matter from 1.1 to 1.3 GHz with ADMX, Phys. Rev. Lett. **135**, 191001 (2025).

[23] C. J. O'Hare, Axionlimits: Data and plots for axion-photon coupling limits, https://github.com/cajohare/AxionLimits (2020).
[24] J. E. Kim, Weak interaction singlet and strong *CP* invariance, Phys. Rev. Lett. **43**, 103 (1979).
[25] M. A. Shifman, A. I. Vainshtein, and V. I. Zakharov, Can confinement ensure natural *CP* invariance of strong interactions?, Nucl. Phys. **B166**, 493 (1980).
[26] A. R. Zhitnitsky, On possible suppression of the axion hadron interactions (in Russian), Sov. J. Nucl. Phys. **31**, 260 (1980), http://inspirehep.net/literature/157263.
[27] S. J. Asztalos, G. Carosi, C. Hagmann, D. Kinion, K. van Bibber, M. Hotz, L. J. Rosenberg, G. Rybka, J. Hoskins, J. Hwang *et al.* (ADMX Collaboration), SQUID-based microwave cavity search for dark-matter axions, Phys. Rev. Lett. **104**, 041301 (2010).
[28] T. Braine *et al.* (ADMX Collaboration), Extended search for the invisible axion with the axion dark matter experiment, Phys. Rev. Lett. **124**, 101303 (2020).
[29] C. Bartram *et al.*, Axion dark matter experiment around 3.3 μev with Dine-Fischler-Srednicki-Zhitnitsky discovery ability, Phys. Rev. Lett. **134**, 111002 (2025).
[30] C. Boutan *et al.* (ADMX Collaboration), Piezoelectrically tuned multimode cavity search for axion dark matter, Phys. Rev. Lett. **121**, 261302 (2018).
[31] C. Bartram *et al.*, Dark matter axion search using a Josephson traveling wave parametric amplifier, Rev. Sci. Instrum. **94**, 044703 (2023).
[32] N. Crisosto, P. Sikivie, N. S. Sullivan, D. B. Tanner, J. Yang, and G. Rybka, ADMX SLIC: Results from a superconducting *LC* circuit investigating cold axions, Phys. Rev. Lett. **124**, 241101 (2020).
[33] S. Lee, S. Ahn, J. Choi, B. R. Ko, and Y. K. Semertzidis, Axion dark matter search around 6.7 μeV, Phys. Rev. Lett. **124**, 101802 (2020).
[34] J. Jeong, S. Youn, S. Bae, J. Kim, T. Seong, J. E. Kim, and Y. K. Semertzidis, Search for invisible axion dark matter with a multiple-cell haloscope, Phys. Rev. Lett. **125**, 221302 (2020).
[35] O. Kwon *et al.* (CAPP Collaboration), First results from an axion haloscope at CAPP around 10.7 μeV, Phys. Rev. Lett. **126**, 191802 (2021).
[36] H. Yoon, M. Ahn, B. Yang, Y. Lee, D. Kim, H. Park, B. Min, and J. Yoo, Axion haloscope using an 18 T high temperature superconducting magnet, Phys. Rev. D **106**, 092007 (2022).
[37] Y. Lee, B. Yang, H. Yoon, M. Ahn, H. Park, B. Min, D. Kim, and J. Yoo, Searching for invisible axion dark matter with an 18 T magnet haloscope, Phys. Rev. Lett. **128**, 241805 (2022).
[38] J. Kim *et al.*, Near-quantum-noise axion dark matter search at CAPP around 9.5 μeV, Phys. Rev. Lett. **130**, 091602 (2023).
[39] A. K. Yi *et al.*, Axion dark matter search around 4.55 μeV with Dine-Fischler-Srednicki-Zhitnitskii sensitivity, Phys. Rev. Lett. **130**, 071002 (2023).
[40] B. Yang, H. Yoon, M. Ahn, Y. Lee, and J. Yoo, Extended axion dark matter search using the CAPP18T haloscope, Phys. Rev. Lett. **131**, 081801 (2023).
[41] J. Kim *et al.*, Near-quantum-noise axion dark matter search at CAPP around 9.5 μeV, Phys. Rev. Lett. **130**, 091602 (2023).
[42] Y. Kim, J. Jeong, S. Youn, S. Bae, K. Lee, A. F. van Loo, Y. Nakamura, S. Oh, T. Seong, S. Uchaikin *et al.*, Experimental search for invisible dark matter axions around 22 μeV, Phys. Rev. Lett. **133**, 051802 (2024).
[43] S. Ahn *et al.*, Extensive search for axion dark matter over 1 GHz with CAPP'S main axion experiment, Phys. Rev. X **14**, 031023 (2024).
[44] S. Bae, J. Jeong, Y. Kim, S. Youn, H. Park, T. Seong, S. Oh, and Y. K. Semertzidis, Search for dark matter axions with tunable TM020 mode, Phys. Rev. Lett. **133**, 211803 (2024).
[45] S. Andriamonje *et al.* (CAST Collaboration), An improved limit on the axion-photon coupling from the CAST experiment, J. Cosmol. Astropart. Phys. 04 (2007) 010.
[46] V. Anastassopoulos *et al.* (CAST Collaboration), New CAST limit on the axion-photon interaction, Nat. Phys. **13**, 584 (2017).
[47] K. Altenmüller *et al.* (CAST Collaboration), New upper limit on the axion-photon coupling with an extended CAST run with a Xe-based micromegas detector, Phys. Rev. Lett. **133**, 221005 (2024).
[48] C. M. Adair *et al.*, Search for dark matter axions with CAST-CAPP, Nat. Commun. **13**, 6180 (2022).
[49] T. Grenet, R. Ballou, Q. Basto, K. Martineau, P. Perrier, P. Pugnat, J. Quevillon, N. Roch, and C. Smith, The Grenoble Axion Haloscope platform (GrAHal): Development plan and first results, arXiv:2110.14406.
[50] B. M. Brubaker *et al.*, First results from a microwave cavity axion search at 24 μeV, Phys. Rev. Lett. **118**, 061302 (2017).
[51] L. Zhong *et al.* (HAYSTAC Collaboration), Results from phase 1 of the HAYSTAC microwave cavity axion experiment, Phys. Rev. D **97**, 092001 (2018).
[52] K. M. Backes *et al.* (HAYSTAC Collaboration), A quantum-enhanced search for dark matter axions, Nature (London) **590**, 238 (2021).
[53] M. J. Jewell *et al.* (HAYSTAC Collaboration), New results from HAYSTAC's phase II operation with a squeezed state receiver, Phys. Rev. D **107**, 072007 (2023).
[54] X. Bai *et al.* (HAYSTAC Collaboration), Dark matter axion search with HAYSTAC phase II, Phys. Rev. Lett. **134**, 151006 (2025).
[55] B. A. d. S. Garcia *et al.*, First search for axion dark matter with a MADMAX prototype, Phys. Rev. Lett. **135**, 041001 (2025).
[56] B. T. McAllister, G. Flower, E. N. Ivanov, M. Goryachev, J. Bourhill, and M. E. Tobar, The ORGAN experiment: An axion haloscope above 15 GHz, Phys. Dark Universe **18**, 67 (2017).
[57] A. P. Quiskamp, B. T. McAllister, P. Altin, E. N. Ivanov, M. Goryachev, and M. E. Tobar, Direct search for dark matter axions excluding ALP cogenesis in the 63- to 67-μeV range with the ORGAN experiment, Sci. Adv. **8**, abq3765 (2022).
[58] A. Quiskamp, B. T. McAllister, P. Altin, E. N. Ivanov, M. Goryachev, and M. E. Tobar, Exclusion of

axionlike-particle cogenesis dark matter in a mass window above 100 μev, Phys. Rev. Lett. **132**, 031601 (2024).
[59] A. P. Quiskamp, G. Flower, S. Samuels, B. T. McAllister, P. Altin, E. N. Ivanov, M. Goryachev, and M. E. Tobar, Near-quantum limited axion dark matter search with the ORGAN experiment around 26 μeV, Phys. Rev. D **111**, 095007 (2025).
[60] D. Alesini *et al.*, Galactic axions search with a superconducting resonant cavity, Phys. Rev. D **99**, 101101 (2019).
[61] D. Alesini *et al.*, Search for invisible axion dark matter of mass $m_a = 43$ μeV with the QUAX $- a\gamma$ experiment, Phys. Rev. D **103**, 102004 (2021).
[62] D. Alesini *et al.*, Search for galactic axions with a high-Q dielectric cavity, Phys. Rev. D **106**, 052007 (2022).
[63] R. Di Vora *et al.* (QUAX Collaboration), Search for galactic axions with a traveling wave parametric amplifier, Phys. Rev. D **108**, 062005 (2023).
[64] A. Rettaroli *et al.* (QUAX Collaboration), Search for axion dark matter with the QUAX–LNF tunable haloscope, Phys. Rev. D **110**, 022008 (2024).
[65] A. A. Melcón *et al.* (CAST Collaboration), First results of the CAST-RADES haloscope search for axions at 34.67 μeV, J. High Energy Phys. 10 (2021) 075.
[66] S. Ahyoune *et al.*, Rades axion search results with a high-temperature superconducting cavity in an 11.7 T magnet, arXiv:2403.07790.
[67] S. DePanfilis, A. C. Melissinos, B. E. Moskowitz, J. T. Rogers, Y. K. Semertzidis, W. U. Wuensch, H. J. Halama, A. G. Prodell, W. B. Fowler, and F. A. Nezrick, Limits on the abundance and coupling of cosmic axions at $4.5 < m_a < 5.0$ μeV, Phys. Rev. Lett. **59**, 839 (1987).
[68] W. Wuensch, S. De Panfilis-Wuensch, Y. K. Semertzidis, J. T. Rogers, A. C. Melissinos, H. J. Halama, B. E. Moskowitz, A. G. Prodell, W. B. Fowler, and F. A. Nezrick, Results of a laboratory search for cosmic axions and other weakly coupled light particles, Phys. Rev. D **40**, 3153 (1989).
[69] H. Chang *et al.* (TASEH Collaboration), First results from the Taiwan axion search experiment with a haloscope at 19.6 μeV, Phys. Rev. Lett. **129**, 111802 (2022).
[70] C. Hagmann, P. Sikivie, N. S. Sullivan, and D. B. Tanner, Results from a search for cosmic axions, Phys. Rev. D **42**, 1297 (1990).
[71] C. Hagmann *et al.*, First results from a second generation galactic axion experiment, Nucl. Phys. B, Proc. Suppl. **51**, 209 (1996).
[72] J. Jeong, S. Youn, S. Ahn, J. E. Kim, and Y. K. Semertzidis, Concept of multiple-cell cavity for axion dark matter search, Phys. Lett. B **777**, 412 (2018).
[73] S. Bae, S. Youn, and J. Jeong, Tunable photonic crystal haloscope for high-mass axion searches, Phys. Rev. D **107**, 015012 (2023).
[74] S. Bae, J. Jeong, Y. Kim, S. Youn, H. Park, T. Seong, S. Oh, and Y. K. Semertzidis, Search for dark matter axions with tunable TM_{020} mode, Phys. Rev. Lett. **133**, 211803 (2024).
[75] J. Kim, S. Youn, J. Jeong, W. Chung, O. Kwon, Y. K. Semertzidis, Exploiting higher-order resonant modes for axion haloscopes, J. Phys. G **47**, 035203 (2020).
[76] J. Jeong, S. Youn, and Y. K. Semertzidis, Horn-array haloscope for volume-efficient broadband axion searches, Phys. Rev. D **108**, L051101 (2023).
[77] A. Caldwell, G. Dvali, B. Majorovits, A. Millar, G. Raffelt, J. Redondo, O. Reimann, F. Simon, and F. Steffen, Dielectric haloscopes: A new way to detect axion dark matter, Phys. Rev. Lett. **118**, 091801 (2017).
[78] P. Brun *et al.* (MADMAX Collaboration), A new experimental approach to probe QCD axion dark matter in the mass range above 40 μeV, Eur. Phys. J. C **79**, 186 (2019).
[79] S. Knirck *et al.* (MADMAX Collaboration), Simulating MADMAX in 3D: Requirements for dielectric axion haloscopes, J. Cosmol. Astropart. Phys. 10 (2021) 034.
[80] J. De Miguel, A. Kryemadhi, and K. Zioutas (On behalf of the DALI Collaboration), Dali sensitivity to streaming axion dark matter, Phys. Rev. D **111**, 023016 (2025).
[81] A. Quiskamp, B. T. McAllister, P. Altin, E. N. Ivanov, M. Goryachev, and M. E. Tobar, Direct search for dark matter axions excluding ALP cogenesis in the 63- to 67- μeV range with the ORGAN experiment, Sci. Adv. **8**, eabq3765 (2022).
[82] A. Quiskamp, B. T. McAllister, P. Altin, E. N. Ivanov, M. Goryachev, and M. E. Tobar, Exclusion of axionlike-particle cogenesis dark matter in a mass window above 100 μeV, Phys. Rev. Lett. **132**, 031601 (2024).
[83] A. P. Quiskamp, G. R. Flower, S. Samuels, B. T. McAllister, P. Altin, E. N. Ivanov, M. Goryachev, and M. E. Tobar, Near-quantum-limited axion dark matter search with the organ experiment around 26 μeV, Phys. Rev. D **111**, 095007 (2025).
[84] A. J. Millar *et al.* (Endorsers Collaboration), Searching for dark matter with plasma haloscopes, Phys. Rev. D **107**, 055013 (2023).
[85] C. Adair *et al.* (CAST-CAPP Collaboration), Search for dark matter axions with CAST-CAPP, Nat. Commun. **13**, 6180 (2022).
[86] D. Ahn *et al.*, High quality factor high-temperature superconducting microwave cavity development for the dark matter axion search in a strong magnetic field, arXiv:1902.04551.
[87] D. Ahn, O. Kwon, W. Chung, W. Jang, D. Lee, J. Lee, S. W. Youn, D. Youm, and Y. K. Semertzidis, Maintaining high Q-factor of superconducting $YBa_2Cu_3O_{7-x}$ microwave cavity in a high magnetic field, arXiv:1904.05111.
[88] D. Ahn, O. Kwon, W. Chung, D. LeeJ. Lee, S. W. YounHeeSu ByunD. Youm, and Y. K. Semertzidis, Biaxially textured $YBa_2Cu_3O_{7-x}$ microwave cavity in a high magnetic field for a dark-matter axion search, Phys. Rev. Appl. **17**, L061005 (2022).
[89] R. Ebadi, D. E. Kaplan, S. Rajendran, and R. L. Walsworth, GALILEO: Galactic axion laser interferometer leveraging electro-optics, Phys. Rev. Lett. **132**, 101001 (2024).
[90] Z. Omarov, J. Jeong, and Y. K. Semertzidis, Speeding axion haloscope experiments using heterodyne-variance-based detection with a power meter, Phys. Rev. D **107**, 103005 (2023).
[91] C. Riek, D. V. Seletskiy, A. S. Moskalenko, J. F. Schmidt, P. Krauspe, S. Eckart, S. Eggert, G. Burkard, and

A. Leitenstorfer, Direct sampling of electric-field vacuum fluctuations, Science **350**, 420 (2015).
[92] C. Riek, P. Sulzer, M. Seeger, A. S. Moskalenko, G. Burkard, D. V. Seletskiy, and A. Leitenstorfer, Subcycle quantum electrodynamics, Nature (London) **541**, 376 (2017).
[93] P. Sikivie, Clean energy from dark matter?, arXiv:2107.14300.
[94] A. Yariv and P. Yeh, *Photonics: Optical Electronics in Modern Communications*, 6th ed. (Oxford University Press, New York, 2006).
[95] B. E. A. Saleh and M. C. Teich, *Fundamentals of Photonics*, 2nd ed. (Wiley-Interscience, New York, 2007).
[96] D. Kim, J. Jeong, S. Youn, Y. Kim, and Y. K. Semertzidis, Revisiting the detection rate for axion haloscopes, J. Cosmol. Astropart. Phys. 03 (2020) 066.
[97] Y. Kim, D. Kim, J. Jeong, J. Kim, Y. C. Shin, and Y. K. Semertzidis, Effective approximation of electromagnetism for axion haloscope searches, Phys. Dark Universe **26**, 100362 (2019).
[98] S. K. Lamoreaux, K. A. van Bibber, K. W. Lehnert, and G. Carosi, Analysis of single-photon and linear amplifier detectors for microwave cavity dark matter axion searches, Phys. Rev. D **88**, 035020 (2013).
[99] G. Oelsner, C. K. Andersen, M. Rehák, M. Schmelz, S. Anders, M. Grajcar, U. Hübner, K. Mølmer, and E. Il'ichev, Detection of weak microwave fields with an underdamped Josephson junction, Phys. Rev. Appl. **7**, 014012 (2017).
[100] L. S. Revin, A. L. Pankratov, A. V. Gordeeva, A. A. Yablokov, I. V. Rakut, V. O. Zbrozhek, and L. S. Kuzmin, Microwave photon detection by an Al Josephson junction, Beilstein J. Nanotechnol. **11**, 960 (2020).
[101] A. D'Elia *et al.*, Stepping closer to pulsed single microwave photon detectors for axions search, IEEE Trans. Appl. Supercond. **33**, 1 (2023).
[102] J. Govenius, R. E. Lake, K. Y. Tan, and M. Möttönen, Detection of zeptojoule microwave pulses using electrothermal feedback in proximity-induced Josephson junctions, Phys. Rev. Lett. **117**, 030802 (2016).
[103] S. Matsuki, I. Ogawa, S. Nakamura, M. Tada, K. Yamamoto, and A. Masaike, Rydberg-atom cavity detector for dark matter axion search in Kyoto, Nucl. Phys. B, Proc. Suppl. **51**, 213 (1996).
[104] K. Kim and J. Ahn, Quantum tomography of Rydberg atom graphs by configurable ancillas, PRX Quantum **4**, 020316 (2023).
[105] A. L. Pankratov *et al.*, Search for dark-matter axions beyond the quantum limit: the cosmological axion sarov haloscope (CASH) proposal, Phys. Rev. D **112**, 035003 (2025).
[106] C. Hagmann, P. Sikivie, N. S. Sullivan, and D. B. Tanner, Results from a search for cosmic axions, Phys. Rev. D **42**, 1297 (1990).
[107] K. Backes *et al.*, A quantum enhanced search for dark matter axions, Nature (London) **590**, 238 (2021).
[108] M. J. Jewell *et al.* (HAYSTAC Collaboration), New results from HAYSTAC's phase II operation with a squeezed state receiver, Phys. Rev. D **107**, 072007 (2023).
[109] B. Yang, H. Yoon, M. Ahn, Y. Lee, and J. Yoo, Extended axion dark matter search using the CAPP18T haloscope, Phys. Rev. Lett. **131**, 081801 (2023).
[110] T. Grenet, R. Ballou, Q. Basto *et al.*, The Grenoble Axion Haloscope platform (GrAHal): Development plan and first results, arXiv:2110.14406.